Observation of two-channel anomalous Hall effect in perpendicularly magnetized $NiCo_2O_4$ epitaxial films

Guowei Zhou,[1,2,*,†] Penghua Kang,[1,*] Huihui Ji,[1] Jiarui Dou,[1] Siqi Wang,[1] and Xiaohong Xu[1,2,‡]

[1]*School of Chemistry and Materials Science, Key Laboratory of Magnetic Molecules and Magnetic Information Materials, Ministry of Education, Shanxi Normal University, Taiyuan 030006, China*

[2]*Research Institute of Materials Science of Shanxi Normal University & Collaborative Innovation Center for Shanxi Advanced Permanent Magnetic Materials and Technology, Taiyuan 030006, China*

(Received 9 February 2023; revised 17 August 2023; accepted 20 September 2023; published 29 September 2023)

The anomalous Hall effect (AHE) is essential for developing highly tunable spintronic devices. An interesting phenomenon with AHE is the appearance of an additional hump on the respective magnetic films. However, it is still being disputed whether it originates from an intrinsic mechanism of the Berry phase accumulation in real space or is artificially generated by inhomogeneities. This work systematically investigates the magnetism, electronic transport, and Hall effect of $NiCo_2O_4$ (NCO) films with different thicknesses. The investigation reveals that the strong perpendicular magnetic anisotropy, metallic transport, and AHE are coexisting in NCO films. Especially, the sharp spikes in anomalous Hall effect are observed in thinner NCO films. The two-channel AHE model is used to explain the origin of the sharp spikes associated with anomalous Hall effect. It indicates that the phase separation is the reason for the sharp spikes. In addition, the mixed valence state, ferrimagnetic order, and the electronic configuration in NCO films are further analyzed. This study is essential for a comprehensive understanding of NCO films.

DOI: 10.1103/PhysRevB.108.094442

I. INTRODUCTION

Transition-metal oxides are well known to be extensively studied for their significant magnetism and transport properties due to the intense interplay of spin, orbit, charge, and lattice [1–3]. Exploring the magnetotransport properties of oxide conductors is worthwhile as it reveals the electronic band structure and scattering mechanism [4]. The anomalous Hall effect (AHE) is one of the magnetotransport properties widely used to investigate the topological properties of magnetic materials. Recently, it has been reported that transverse Hall voltages are generated in addition to the ordinary Hall effect (OHE) and AHE. As a result, a Hall effect is observed, called topological Hall effect (THE) [5–7]. The visual appearance in magnetic materials is a hump in Hall resistivity in addition to OHE and AHE. It is attributed to the presence of magnetic skyrmions due to the Dzyaloshinskii-Moriya interaction (DMI). Generally, the DMI is caused by strong spin-orbit coupling (SOC) and the breaking of inversion symmetry [8,9]. The typical systems include intrinsic $SrRuO_3$ (SRO), $SrIrO_3$ (SIO), and metal multilayers [10–12].

In SRO/SIO superlattices and ferromagnet-heavy metal multilayers, it is well known that the interfacial DMI can be generated due to SOC and the breaking of inversion symmetry. Therefore, magnetic skyrmions and noncollinear magnetic structures are formed, for which the direct manifestation is the presence of humps associated with AHE [8,13–16]. It is attributed to the existence of THE. However, the origin of the hump anomaly in single-layer SRO is controversial [8–11,17]. The unusual peaks in the Hall resistivity of ultrathin SRO films in numerous studies are attributed to nontrivial spin configurations with spin chirality [18]. In other words, the hump originates from the real-space Berry phase. The source of the spin chirality is due to the DMI-driven skyrmions. Moreover, in strongly correlated systems, inhomogeneous phases are crucial in the excitation of rich physical phenomena [19,20]. Some factors such as defects are usually unavoidable in the preparation of films [21]. Wang and Kimbell *et al.* used a two-channel AHE model to explain the unusual hump associated with AHE [10,17]. It is caused by the superposition of two AHEs of opposite signs in the k-space Berry curvature [22]. It indicates that the inhomogeneities dominate the abnormal magnetotransport properties [10,17]. In Mn-doped topological insulator Bi_2Se_3, the sign of the anomalous Hall resistance changes from positive to negative as the concentration of Mn increases due to the effect of magnetic dopants on the surface and bulk states of the topological insulator [23].

Inverse spinel $NiCo_2O_4$ (NCO) is a ferrimagnetic conductor. Its Curie temperature is above 395 K [24]. The high sensitivity of NCO to growth parameters such as temperature, oxygen partial pressure, and thickness is of great concern [25–27]. Theoretical calculations show that the density of states at the Fermi level (E_F) of NCO is determined by the minority spin subband, leading to half-metallic properties [28–30]. Moreover, a band crossing near the E_F of NCO is the source of the Berry curvature [31,32]. Therefore, the investigations on temperature- or thickness-dependent AHE sign reversal and on topological Hall effect like features are highly necessary, and understanding the underlying mechanism in NCO film is very urgent at present [24,33].

*These authors contributed equally to this paper.
†zhougw@sxnu.edu.cn
‡xuxh@sxnu.edu.cn

In this work, the single-layer NCO films with different thicknesses are prepared by a pulsed laser deposition system. The relevant magnetism, electronic transport, and Hall effect are comprehensively investigated. The sharp spikes associated with AHE is first observed in metallic NCO with perpendicular magnetic anisotropy (PMA). The origin of this sharp spikes associated with anomalous Hall effect is explained by a two-channel AHE model. In addition, the valence state, magnetic order, and the electronic configurations of NCO films have also been explored. This investigation provides critical information for understanding the AHE of NCO films.

II. EXPERIMENTAL SECTION

NCO thin films with various thicknesses were deposited on (001)-oriented single crystal $MgAl_2O_4$ (MAO) substrates ($2.5 \times 5 \times 0.5\,mm^3$) by a pulsed laser deposition system (PLD, Neocera). The substrate temperature and oxygen partial pressure were 375 °C and 150 mTorr. A stoichiometric NCO ceramic target was ablated by KrF excimer laser (Coherent) with a wavelength of 248 nm. Laser energy and repetition frequency were set to 360 mJ and 5 Hz. Subsequently, the samples were annealed under 100 Torr oxygen pressure for 30 min to ensure the high quality of the film and then cooled to room temperature. Owing to the high rate of laser pulses, the NCO films of different thicknesses were prepared by controlling the number of pulses. A profilometer measured the thicknesses to be 30, 15, and 7 nm (P-7, KLA-Tencor).

The crystal structure and reciprocal space mapping (RSM) images of NCO film were determined by high-resolution x-ray diffraction (HR-XRD, Bruker) with a Cu $K\alpha$ wavelength of 0.15 406 nm. The film surface was characterized by atomic force microscopy (AFM, Bruker). The cross-sectional sample of NCO film was prepared using focused ion beams (FIBs). High-angle annular dark-field scanning transmission electron microscopy (HAADF-STEM, JEOL ADF1) was used to take the interface structure image at room temperature with a spherical aberration corrector. The operating voltage was 300 kV. The dependence of magnetization on magnetic field and temperature was determined in vibrating sample magnetometry (VSM) mode by a physical property measurement system (PPMS, Quantum Design). The electronic transport and magnetotransport of NCO films were characterized in resistivity mode by four-point probe and van der Pauw measurements. The contacts between the film and electrode were done by ultrasonic Al-wire bonding. The cation valence state was recorded by x-ray photoelectron spectroscopy (XPS, K-Alpha, Thermo Fisher) with an Al $K\alpha$ x-ray source. X-ray absorption spectra (XAS) with different circularly polarized light for Co $L_{2,3}$ and Ni $L_{2,3}$ edges in the total electron yield (TEY) mode were collected at the BL08U1A beamlines in Shanghai Synchrotron Radiation Facility (SSRF). The difference between the spectra was normalized to express the x-ray magnetic circular dichroism (XMCD) signal.

III. RESULTS AND DISCUSSION

A. Structure and surface characterizations of NCO films

NCO films were epitaxially grown on single crystal (001)-oriented MAO substrates via PLD. The bulk cubic lattice

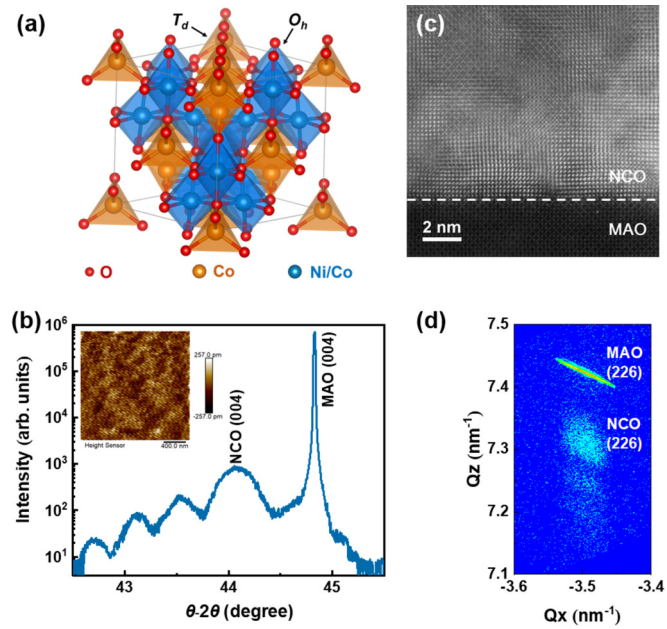

FIG. 1. (a) Crystal structure of inverse spinel NCO. There are 8 T_d sites and 16 O_h sites per unit cell. The red sphere is O element, the brown sphere is Co element, and the blue sphere is Ni or Co elements. (b) HR-XRD θ-2θ scan data of 30-nm NCO film on MAO substrates around (004) symmetric reflections. The inset shows the surface topography of 7-nm NCO film. (c) HAADF-STEM image showing the interface at a scale of 2 nm for 30-nm NCO film. The interface is sharp and well defined. (d) RSM of the 30-nm NCO film. The maps are recorded in the (226) MAO reflection.

constants for NCO and MAO are 0.8114 and 0.8033 nm, respectively. There is an in-plane compressive strain of −0.38% for NCO films. Figure 1(a) displays the schematic diagram of the crystal structure of NCO. In inverse spinel NCO, the Ni cations occupy the octahedral (O_h) sites, and Co cations are evenly distributed between the octahedral and tetrahedral (T_d) sites. The inset of Fig. 1(b) shows an AFM image of 7 nm NCO film at a preselected region ($2 \times 2\,\mu m^2$). The root-mean-square roughness is only 0.0731 nm. Hence, the NCO film surface is smooth and flat. The HR-XRD pattern of 30 nm NCO film is shown in Fig. 1(b). The positions of NCO (004) and MAO (004) peaks are 44.07 ° and 44.81 °, respectively, which is consistent with previous reports on NCO films [24–26].

Furthermore, the NCO (004) peak is located to the left of MAO (004), indicating tensile stress on the NCO film from the MAO substrate. It also indicates the high quality of the prepared film because of the periodic Laue oscillations around the NCO (004) peak. In addition, the microscopic structure of the interface between substrate and film was further observed by HAADF-STEM. Figure 1(c) and Fig. S1a of the Supplemental Material [34] show the HAADF-STEM images of 30-nm NCO film at different scales. The images illustrate that NCO film can be grown coherently on an MAO substrate without diffusion and with a sharp interface. The RSM around (226) reflection of 30-nm NCO film shown in Fig. 1(d) verifies the epitaxial growth of NCO films. It is in agreement with the results in Figs. 1(b) and 1(c).

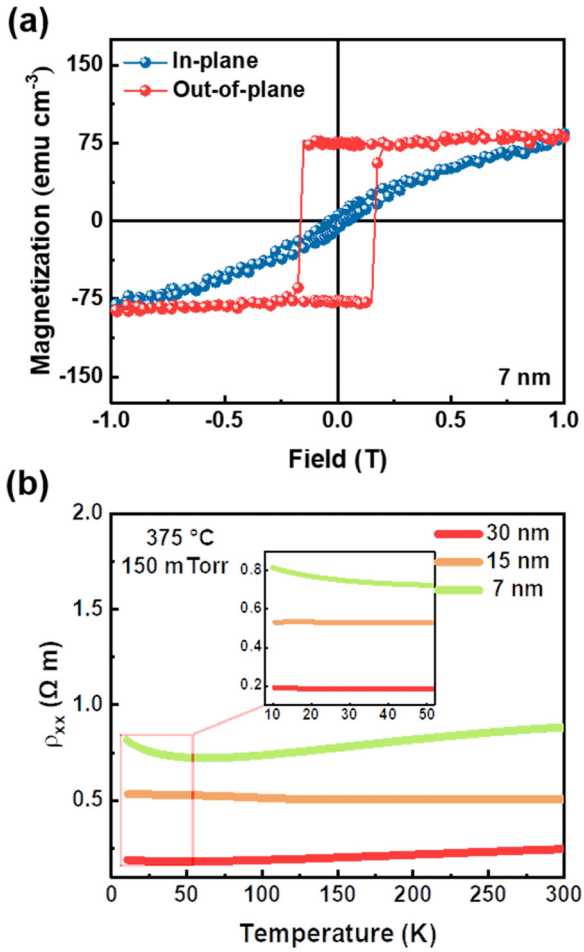

FIG. 2. (a) Magnetic-field-dependent magnetization of 7-nm NCO film measured at 5 K with a magnetic field of 1.0 T. The red and blue curves denote the OOP and IP field configurations. (b) Temperature-dependent resistivity for NCO films with various thicknesses measured from 10 to 300 K. The inset displays an enlarged image of the temperature-dependent resistivity measured from 10 to 50 K.

B. Magnetic anisotropy and electronic transport of NCO films

Based on our previous investigation of the room-temperature PMA in 30-nm single-layer NCO films [27], which is attributed to the compressive strain by the MAO substrates, this work further explored the dependence of magnetic anisotropy on thickness. Figure 2(a) displays the hysteresis loop of 7-nm NCO film applied in plane (IP) and out of plane (OOP) magnetic field measured at 10 K. It indicates that the PMA is observed in NCO film. Furthermore, temperature-dependent magnetization applied an OOP magnetic field for NCO films with different thicknesses as shown in Fig. S3 of the Supplemental Material [34]. Obviously, there is no magnetic compensation temperature in NCO films similar to that of the generally ferrimagnetic materials [12,35,36].

The dependence of electronic transport of NCO film on thickness measured from 10 to 300 K is shown in Fig. 2(b). It is evident that the resistance gradually increases with the decrease in the film thickness. Moreover, as the temperature decreases, the resistance first decreases monotonically up to 50 K temperature and then increases slightly. It indicates that NCO films of different thicknesses exhibit metallic behavior. In contrast to previous reports, these samples did not show a metal-insulator transition at elevated temperatures [25,37]. The inset of Fig. 2(b) is an enlarged image of temperature-dependent resistance measured from 10 to 50 K. The minimum resistance value at about 50 K is due to the localization of charge carriers induced by cation disorder in the NCO film [25,26]. The experimental result is consistent with investigations of theoretical models [37,38]. Therefore, the PMA and metallic transport coexisted in NCO films with various thicknesses, which is significant for developing spintronic devices.

C. Magnetotransport of NCO films

In the following, we focus on the dependence of the Hall effect in NCO films on two degrees of freedom, including thickness and temperature. Figures 3(a)–3(c) display the AHE of NCO films with thicknesses of 30, 15, and 7 nm for various temperatures. The measured curves are arranged vertically in Figs. S4(a)–4(c) of the Supplemental Material [34] to enhance the visibility of the data. In the processing of the raw data, the total Hall resistivity was obtained by $\rho_{xy} = (\rho_{\mathrm{H}} - \rho_{-\mathrm{H}})/2$, where ρ_{H} and $\rho_{-\mathrm{H}}$ are the resistivity of the positive and negative sweep fields, respectively. In addition, because the Lorentz force causes the OHE, the contribution of OHE has been removed from the ρ_{xy}. The expression for the Hall resistivity is

$$\rho_{xy} = \rho_{xy}^{\mathrm{OHE}} + \rho_{xy}^{\mathrm{AHE}} \tag{1}$$

with $\rho_{xy}^{\mathrm{OHE}} = r_{\mathrm{O}} \times \mu_{\mathrm{O}} H$ and $\rho_{xy}^{\mathrm{AHE}} = 4\pi \mathrm{r}_{\mathrm{A}} M$. Here, the Hall resistivity ρ_{xy} has two terms, ordinary Hall resistivity ρ_{xy}^{OHE} and anomalous Hall resistivity ρ_{xy}^{AHE}. The r_{O} and r_{A} are the ordinary and anomalous Hall coefficients, respectively. The r_{A} depends on the intrinsic properties of the material and the longitudinal conductivity [22]. The H and M are applied magnetic field and OOP magnetization, respectively. The linear field dependence of ρ_{xy} at high fields indicates single-type charge carrier transport and magnetic saturation [39]. Thus, the ρ_{xy}^{AHE} is obtained by subtracting the ρ_{xy}^{OHE} from the ρ_{xy}. Furthermore, the AHE is proportional to the OOP magnetization. It is worth emphasizing that the AHE is compelling evidence that magnetic materials possess PMA. In Figs. 3(a)–3(c), temperature-dependent AHEs in NCO films with various thicknesses display hysteretic behavior with rather large coercive and saturation field at all temperatures. Also, the magnitudes of remanent magnetization and saturation magnetization are equal. Therefore, the AHE results are consistent with the hysteresis loops presented in Fig. 2(a) and Fig. S2 of the Supplemental Material [34]. It further confirms the PMA of the NCO films with different thicknesses. Figures 3(d) and 3(e) show the temperature-dependent coercive field (H_{C}, left) and the absolute value of ρ_{xy} ($|\rho_{xy}|$, right) extracted from the AHE in 30- and 15-nm NCO films. The $|\rho_{xy}|$ decreases with decreasing temperature, and the H_{C} increases. Similar changes at the high temperature region were also observed in the 7-nm NCO film shown in Fig. 3(f). In contrast, the $|\rho_{xy}|$ increases with a decrease in the temperature in the low-temperature region. Particularly, the sign of AHE

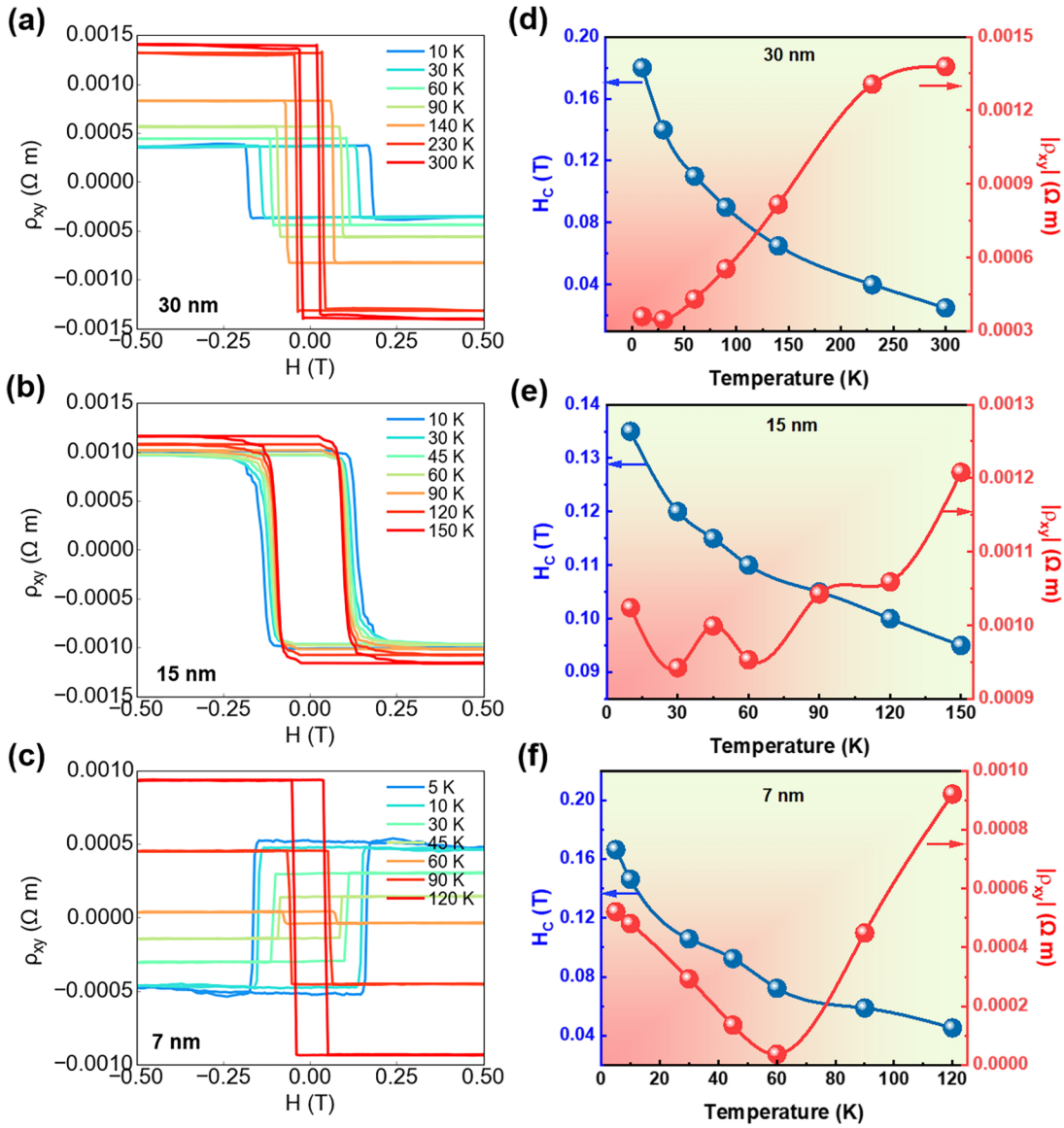

FIG. 3. Temperature-dependent AHE for NCO films with thicknesses of (a) 30, (b) 15, and (c) 7 nm. Temperature-dependent H_C (left) and the $|\rho_{xy}|$ (right) extracted from the AHE with thicknesses of (d) 30, (e) 15, and (f) 7 nm. The blue and red lines are H_C-T and $|\rho_{xy}|$-T curves, respectively.

in 7-nm NCO film changes from negative to positive between 45 and 60 K with decreasing temperature [Fig. 3(c)]. For the positive or negative sign of AHE, the curves in alignment with the hysteresis loops are taken as positive (anticlockwise), and negative (clockwise) otherwise.

To explore the reason and critical temperature for the ρ_{xy} sign change in 7-nm NCO film, as shown in Fig. 4(a), the dependence of AHE on temperature from 50 to 59 K is further measured. Owing to the small range of test temperature gradients, the change of H_C is negligible. The critical temperature for the AHE sign reversal is 57 K. The AHE is negative above 57 K and positive below 57 K. Also, the ρ_{xy} reaches the minimum value at 57 K. Remarkably, there are sharp spikes associated with AHE appearing near the H_C in the temperature range 52–58 K. Interestingly, the sharp spikes vanish at other temperatures. The size of the sharp spikes is defined with the amplitude extracted and summarized in Fig. S5d of the Supplemental Material [34]. The amplitude representing the size of the sharp spikes increases with increasing temperature, reaching a maximum value of 57 K. This amplitude then decreases with a further increase in temperature. The maximum value of the amplitude at 57 K is about $3.12\times\ 10^{-5}\,\Omega\,\mathrm{m}$. In addition, the amplitude representing the size of the sharp spikes is antisymmetric at temperatures from 52 to 58 K. The values of their magnitudes are close to each other, but have opposite signs in positive and negative magnetic fields. Here, the Hall resistivity corresponds to the following expression:

$$\rho_{xy} = \rho_{xy}^{OHE} + \rho_{xy}^{AHE} + \rho_{xy}^{Amp.}, \tag{2}$$

where $\rho_{xy}^{Amp.}$ is the amplitude. So, the amplitude is obtained by subtracting the ρ_{xy}^{AHE} and ρ_{xy}^{OHE} terms from the ρ_{xy}. For clarity, the schematic diagram of extracted amplitude is shown in the inset of Fig. S5d of the Supplemental Material [34]).

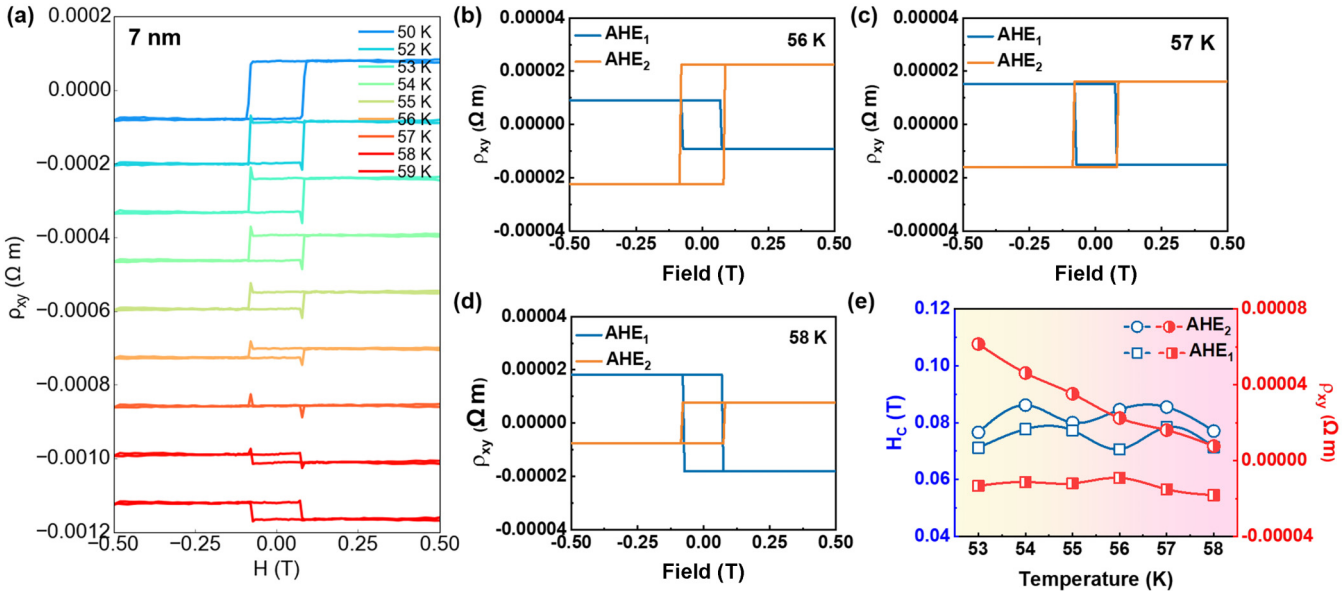

FIG. 4. (a) Temperature-dependent AHE for 7-nm NCO film measured from 50 to 59 K. The data are shifted vertically for clarity. ρ_{xy}-H curves show the sharp spikes from 52 to 58 K. The two-channel AHE model fits the AHE of 7-nm NCO film at (b) 56, (c) 57, and (d) 58 K. The two components fit at different temperatures. The blue and orange curves are positive (AHE_2) and negative (AHE_1) fitting curves, respectively. (e) Temperature-dependent H_C (left) and ρ_{xy} (right) extracted from the two AHE components. The blue and red dotted lines are H_C-T and ρ_{xy}-T curves of AHE_2 (open and semi-open circles) and AHE_1 (open and semi-open squares), respectively.

Now, let us explore the mechanism of the sharp spikes and change of sign in AHE. Inverse spinel NCO has a complex crystal structure. NCO is an intrinsically disordered material because Ni and Co cations are randomly distributed or occupy O_h and T_d sites [40–43]. In other words, NCO has a nonunitary valence state. So, the phase separation is easily generated during the preparation of NCO films due to the sensitivity to the growth parameters set by pulsed laser deposition. However, the phase separation is not detected by HR-XRD or HAADF-STEM, and no steplike hysteresis loop is observed. Moreover, it is confirmed by increasing the resistivity below 50 K and the buckling in the hysteresis loops at 2 K and lower temperatures [25,42].

As per the previous investigation, the NCO is a multiband conductor [44]. Chen *et al.* studied the dependence of the effective carrier density on temperature by extracting the ordinary Hall coefficient, ruling out a direct correlation between the sign change and carrier types [24]. Furthermore, they reported that the scaling laws of the anomalous conductivity (σ_{xy}) and longitudinal conductivity (σ_{xx}) satisfied the relation $\sigma_{xy} = \sigma_{xy}^{(0)} + A\sigma_{xx}^{1.6}$ to explain the change of sign of AHE in NCO [33]. It shows that the intrinsic Berry curvature of the band and the skew scattering mechanism determines the AHE in NCO films. Also, the side jump mechanism also contributes to AHE for extremely thin NCO films. Afterwards, Kan *et al.* found that the anomalous Hall conductivity σ_{AHE} is constant when σ_{xx} is sufficiently high. In contrast, when σ_{xx} is low, the scaling relationship is $\sigma_{AHE} \sim \sigma_{xx}^{1.6}$ [45]. It indicates that the crossover of Berry curvature and impurity scatterings determines AHE in NCO film.

Since the SOC and inversion symmetry breaking in NCO films can be neglected, there are no DMI and skyrmions in NCO films. So, we conjecture that the sharp spikes associated with the AHE of NCO film is caused by the phase separation and may be explained by the two-channel AHE model. The two-channel AHE model was proposed by Gerber and by Kan *et al.* in 2018 [46,47]. The expression is as follows:

$$\rho_{xy} = \rho_{xy}^{OHE} + \rho_{AHE_1} + \rho_{AHE_2}, \tag{3}$$

where $\rho_{AHE_1} = \rho_{s_1} * \tanh[(H \pm H_{C_1})/H_{O_1}]$ and $\rho_{AHE_2} = \rho_{s_2} * \tanh[(H \pm H_{C_2})/H_{O_2}]$. In the two AHE components, ρ_{s_1} and ρ_{s_2} are the coefficients of two terms. H_{O_1} and H_{O_2} are constants. H_{C_1} and H_{C_2} are for coercivity. It suggests that the ρ_{xy} is the sum of ρ_{xy}^{OHE} and two opposite-sign AHEs. Figures 4(b)–4(d) and Figs. S5(a)–S5(c) of the Supplemental Material [34] show the AHE of 7-nm NCO film in the temperature range 52–58 K fitted by the two-channel AHE model. The dependence of the H_C (left) and ρ_{xy} (right) on temperature extracted from the two AHE components is summarized in Fig. 4(e). It shows that the magnitude of the H_C in the two AHEs is almost equal. The resistivity of AHE_2 decreases with increasing temperature, while the resistivity of AHE_1 is almost constant.

Interestingly, the $|\rho_{xy}|$ in both terms is approximately equal to $1.5\times 10^{-5}\,\Omega\,m$ at 57 K. Therefore, the AHE of NCO film is generated by the superposition of two AHEs of opposite signs. In other words, the phase separation exists in NCO film. Regarding the origin of the phase separation, the schematic diagrams of thicker and thinner samples are shown in Fig. S8 of the Supplemental Material [34]. In general, the strain relaxation state of films prepared on rigid substrates is considered to be closely associated with the film thickness [10,17,48]. As the thickness of the film increases, the stresses on the film are released. As a result, the crystal structure of the thicker films is close to a perfect inverse spinel (left panel), while the thinner films are in a state of global strain. Therefore, the interface between film and substrate is more prone to phase separation in the thinner films (right panel). In addition, since there is no

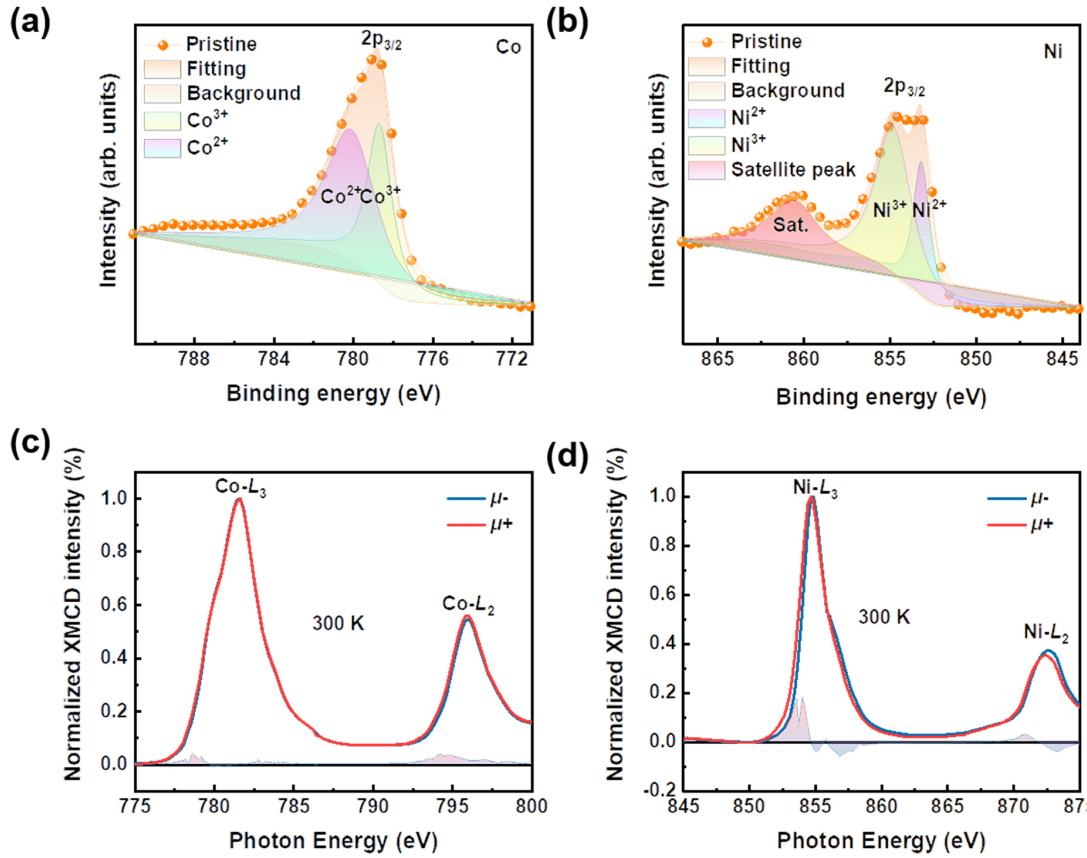

FIG. 5. XPS spectra of (a) Co $2p_{3/2}$ core level and (b) Ni $2p_{3/2}$ core level for 30-nm NCO film. XAS of (c) Co and (d) Ni edges for 30-nm NCO film under a 0.25-T magnetic field at 300 K. The color fill is obtained by subtracting $\mu-$ (red line) from $\mu+$ (blue line), which is the XMCD signal.

magnetic compensation temperature for ferrimagnetic NCO and the concentration of Ni cations plays a dominant role in the transport properties of NCO films [42,49], we discuss the concentration of Ni with various valence states in NCO films with different thicknesses in the next section.

D. X-ray photoelectron spectrum and x-ray magnetic circular dichroism in NCO films

To investigate the valence states of Ni and Co cations in NCO films, x-ray photoelectron spectroscopy (XPS) was done on Co $2p_{3/2}$ and Ni $2p_{3/2}$, as shown in Figs. 5(a) and 5(b). The binding energy position of the elements was calibrated using the reference C 1s photoelectron signal at 284.8 eV. The XPS spectra were deconvoluted into subpeaks using the Voigt function, which was then assigned to a specific valence state. In the Co $2p_{3/2}$ core level peak, two deconvoluted subpeaks at 781.0- and 779.5-eV binding energies correspond to Co^{2+} and Co^{3+}. Similarly, according to the Ni $2p_{3/2}$ peaks with appropriate curve-fitting lines, the satellite peaks, Ni^{2+} and Ni^{3+}, associated with binding energies 861.3, 855.6, and 854.0 eV, are observed. These results agree well with the previous reports [50,51]. The peak area ratios for Co^{3+} and Co^{2+} are 0.48. The peak area ratios for Ni^{3+} and Ni^{2+} are 2.36. It confirms the mixed valence state in NCO and the higher content of Co^{2+} and Ni^{3+}. In addition, the concentration of Ni with various valence states in NCO films with different thicknesses was measured in Fig. S9 of the Supplemental Material [34]. The Ni^{3+} to Ni^{2+} ratios for the 15- and 7-nm NCO films were obtained from the fitted peak area ratios as 2.27 and 2.19. Therefore, the concentration of Ni^{2+} increases as the film thickness decreases. It is the source of phase separation in film, which in turn confirms the sign reversal and sharp spikes near the coercive field in the AHE of thinner films.

Moreover, to explore the possible magnetic order of NCO films, x-ray magnetic circular dichroism (XMCD) measurements were performed. Figures 5(c) and 5(d) and Fig. S10 of the Supplemental Material [34] show the x-ray absorption spectra (XAS) of circularly polarized light for Co $L_{2,3}$ and Ni $L_{2,3}$ edges at 300 and 100 K along different orientations relative to the sample surface. In addition, a magnetic field of 0.25 T was applied while taking the measurements. The apparent difference between the two spectra is the XMCD signal which is $\mathrm{XMCD} = \mathrm{XAS}_{\mathrm{left}}\,(\mu^{+}) - \mathrm{XAS}_{\mathrm{right}}\,(\mu^{-})$. It demonstrates that the magnetic moments of Ni and Co are antiferromagnetically coupled and have a net magnetic moment. Therefore, there is ferrimagnetic order in NCO films, which is consistent with previous studies [42].

E. Electronic configurations in NCO films

Based on this study of mixed valence state and ferrimagnetic order in NCO film, the possible electronic configurations are discussed now. In the ideal NCO, the valence state of Ni

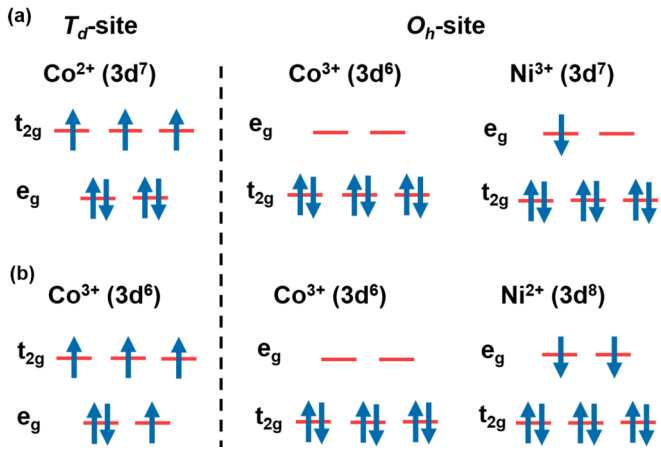

FIG. 6. The electronic configurations of Ni and Co cations in NCO films. (a) The valence state of Co at the T_d site and O_h site is +2 and +3, respectively. The valence state of Ni at the O_h site is +3. (b) The valence state of Co at both the T_d and O_h sites is +3. The valence state of Ni at the O_h site is +2.

at the O_h site is +2, while the Co at both T_d and O_h sites is +3. However, defects such as oxygen vacancies are formed in films during preparation due to the growth conditions. So, the mixed valence state in this paper should be caused by the emergence of specific amounts of Ni^{3+} and Co^{2+} in the O_h and T_d sites, respectively. Following this line of thought, two possible electronic configurations of NCO are shown in Fig. 6. First, the Co^{2+} and Co^{3+} occupy the T_d and O_h sites, while the Ni^{3+} is located at the O_h site [Fig. 6(a)]. Second, the valence state of Co at both the T_d and O_h sites is +3, while the valence state of Ni at the O_h site is +2 [Fig. 6(b)]. Therefore, the valence composition of NCO can be expressed as $[Co^{2+}_{1-x}Co^{3+}_{x}]_{T_d}[Co^{3+}Ni^{2+}_{x}Ni^{3+}_{1-x}]_{O_h}O_4^{2-}$ [51–53]. Overall, the T_d-site Co and the O_h-site Ni are antiparallelly coupled and contribute to the magnetism, with a net magnetic moment of $2\mu_B$ per f.u. Moreover, regarding the cation contribution to the magnetic properties of NCO films, Co at the T_d site plays a dominant role, Ni at the O_h site contributes less, and Co at the O_h site does not contribute to magnetism. These results are consistent with previous research studies [30].

IV. CONCLUSIONS

In summary, we have studied in detail the dependence of magnetic properties, electronic transport, and magnetotransport on the thickness of NCO films. Consistently, the NCO films of various thicknesses exhibit strong PMA and metallic conductivity. Furthermore, the AHE results further confirm the presence of PMA in NCO. In contrast, the AHE sign in 30- and 15-nm NCO films is negative at various temperatures. On the contrary, the AHE sign in 7-nm NCO film is positive below 57 K. It is attributed to the fact that a combination of intrinsic Berry curvature and impurity scattering determines the AHE in NCO. In addition, an exciting feature, the appearance of sharp spikes, is observed associated with the AHE. Unlike the well-known topological Hall effect induced by DMI and skyrmions, we used a two-channel AHE model to investigate the origin of the sharp spikes. It indicates that the phase separation causes the sharp spikes associated with AHE. Although the exact source of the phases requires detailed research, we believe it is crucial to explain the AHE in NCO with a two-channel AHE model. The XPS and XMCD results also indicate mixed valence sate and ferrimagnetic order in NCO films. We have also discussed two possible electronic configurations of NCO. The results show that the T_d-site Co plays a dominant role in the magnetic properties, while the O_h-site Ni contributes less. Observation of sharp spikes associated with AHE does not give unequivocal evidence for THE possibly due to the phase separation. Thus, it is necessary to exclude the influence of these factors in exploring THE and to distinguish the genuine and mimicked THE.

ACKNOWLEDGMENTS

This work was financially supported by the National Natural Science Foundation of China (Grants No. 51901118, No. 51871137, No. 12174237, and No. 52171183), the 1331 Engineering of Shanxi Province, the Research Project Supported by Shanxi Scholarship Council of China (Project No. 2021–093), and the Scientific and Technological Innovation Programs of Higher Education Institutions in Shanxi (Grant No. 2020L0237). We acknowledge the XAS measurement at Beamline BL08U1A in the Shanghai Synchrotron Radiation Facility (SSRF) and the XLD measurement at Beamline BL12-a in the National Synchrotron Radiation Laboratory (NSRL).

[1] A. Ohtomo and H. Y. Hwang, A high-mobility electron gas at the $LaAlO_3/SrTiO_3$ heterointerface, Nature (London) **427**, 423 (2004).

[2] R. Scherwitzl, S. Gariglio, M. Gabay, P. Zubko, M. Gibert, and J. M. Triscone, Metal-insulator Transition in Ultrathin $LaNiO_3$ Films, Phys. Rev. Lett. **106**, 246403 (2011).

[3] N. Reyren, S. Thiel, A. D. Caviglia, L. F. Kourkoutis, G. Hammerl, C. Richter, C. W. Schneider, T. Kopp, A. S. Rüetschi, D. Jaccard, M. Gabay, D. A. Muller, J. M. Triscone, and J. Mannhart, Superconducting interfaces between insulating oxides, Science **317**, 1196 (2007).

[4] X. Xu, C. Mellinger, Z. G. Cheng, X. Chen, and X. Hong, Epitaxial $NiCo_2O_4$ film as an emergent spintronic material: Magnetism and transport properties, J. Appl. Phys. **132**, 020901 (2022).

[5] Y. Ohuchi, J. Matsuno, N. Ogawa, Y. Kozuka, M. Uchida, Y. Tokura, and M. Kawasaki, Electric-field control of anomalous and topological Hall effects in oxide bilayer thin films, Nat. Commun. **9**, 213 (2018).

[6] Q. Qin, L. Liu, W. Lin, X. Shu, Q. Xie, Z. Lim, C. Li, S. He, G. M. Chow, and J. Chen, Emergence of topological Hall effect in a $SrRuO_3$ single layer, Adv. Mater. **31**, 1807008 (2019).

[7] P. Zhang, A. Das, E. Barts, M. Azhar, L. Si, K. Held, M. Mostovoy, and T. Banerjee, Robust skyrmion-bubble textures in $SrRuO_3$ thin films stabilized by magnetic anisotropy, Phys. Rev. Res. **2**, 032026(R) (2020).

[8] J. Matsuno, N. Ogawa, K. Yasuda, F. Kagawa, W. Koshibae, N. Nagaosa, Y. Tokura, and M. Kawasaki, Interface-driven topological Hall effect in $SrRuO_3$-$SrIrO_3$ bilayer, Sci. Adv. **2**, e1600304 (2016).

[9] L. Wang, Q. Feng, Y. Kim, R. Kim, K. H. Lee, S. D. Pollard, Y. J. Shin, H. Zhou, W. Peng, D. Lee, W. Meng, H. Yang, J. H. Han, M. Kim, Q. Lu, and T. W. Noh, Ferroelectrically tunable magnetic skyrmions in ultrathin oxide heterostructures, Nat. Mater. **17**, 1087 (2018).

[10] L. Wang, Q. Feng, H. G. Lee, E. K. Ko, Q. Lu, and T. W. Noh, Controllable thickness inhomogeneity and Berry curvature engineering of anomalous Hall effect in $SrRuO_3$ ultrathin films, Nano Lett. **20**, 2468 (2020).

[11] K. Y. Meng, A. S. Ahmed, M. Baćani, A. O. Mandru, X. Zhao, N. Bagués, B. D. Esser, J. Flores, D. W. McComb, H. J. Hug, and F. Yang, Observation of nanoscale skyrmions in $SrIrO_3/SrRuO_3$ bilayers, Nano Lett. **19**, 3169 (2019).

[12] Z.-Y. Xiao, Z.-Y. Quan, W. Zhang, D. Li, H.-H. Liu, G.-W. Zhou, J. Zhang, F. Zhang, X. Liu, X.-H. Xu, and M.-Z. Wu, Experimental observation of topological Hall effects in compensated ferrimagnet-heavy metal layered structures, Sci. China Phys. Mech. **64**, 287511 (2021).

[13] D. Zheng, Y. W. Fang, S. Zhang, P. Li, Y. Wen, B. Fang, X. He, Y. Li, C. Zhang, W. Tong, W. Mi, H. Bai, H. N. Alshareef, Z. Q. Qiu, and X. Zhang, Berry phase engineering in, $SrRuO_3/SrIrO_3/SrTiO_3$ superlattices induced by band structure reconstruction, ACS Nano **15**, 5086 (2021).

[14] A. Fert, V. Cros, and J. Sampaio, Skyrmions on the track, Nat. Nanotechnol. **8**, 152 (2013).

[15] S. Woo, K. Litzius, B. Krüger, M. Y. Im, L. Caretta, K. Richter, M. Mann, A. Krone, R. M. Reeve, M. Weigand, P. Agrawal, I. Lemesh, M. A. Mawass, P. Fischer, M. Kläui, and G. S. Beach, Observation of room-temperature magnetic skyrmions and their current-driven dynamics in ultrathin metallic ferromagnets, Nat. Mater. **15**, 501 (2016).

[16] M. V. Sapozhnikov, N. S. Gusev, S. A. Gusev, D. A. Tatarskiy, Y. V. Petrov, A. G. Temiryazev, and A. A. Fraerman, Direct observation of topological Hall effect in Co/Pt nanostructured films, Phys. Rev. B **103**, 054429 (2021).

[17] G. Kimbell, P. M. Sass, B. Woltjes, E. K. Ko, T. W. Noh, W. D. Wu, and J. W. A. Robinson, Two-channel anomalous Hall effect in $SrRuO_3$, Phys. Rev. Mater. **4**, 054414 (2020).

[18] K. Everschor-Sitte and M. Sitte, Real-space Berry phases: Skyrmion soccer, J. Appl. Phys. **115**, 172602 (2014).

[19] E. Dagotto, Complexity in strongly correlated electronic systems, Science **309**, 257 (2005).

[20] N. Mathur and P. Littlewood, Mesoscopic texture in manganites, Phys. Today **56**(1), 25 (2003).

[21] P. Roy, A. Carr, T. Zhou, B. Paudel, X. Wang, D. Chen, K. T. Kang, A. Pateras, Z. Corey, S. Lin, J. X. Zhu, M. V. Holt, J. Yoo, V. Zapf, H. Zeng, F. Ronning, Q. Jia, and A. Chen, Origin of topological Hall-like feature in epitaxial $SrRuO_3$ thin films, Adv. Electron. Mater. **9**, 2300020 (2023).

[22] N. Nagaosa, J. Sinova, S. Onoda, A. H. MacDonald, and N. P. Ong, Anomalous hall effect, Rev. Mod. Phys. **82**, 1539 (2010).

[23] N. Liu, J. Teng, and Y. Li, Two-component anomalous Hall effect in a magnetically doped topological insulator, Nat. Commun. **9**, 1282 (2018).

[24] X. Chen, X. Zhang, M. G. Han, L. Zhang, Y. Zhu, X. Xu, and X. Hong, Magnetotransport anomaly in room-temperature ferrimagnetic $NiCo_2O_4$ thin films, Adv. Mater. **31**, 1805260 (2019).

[25] P. Silwal, L. Miao, I. Stern, X. Zhou, J. Hu, and D. Ho Kim, Metal insulator transition with ferrimagnetic order in epitaxial thin films of spinel $NiCo_2O_4$, Appl. Phys. Lett. **100**, 032102 (2012).

[26] P. Silwal, L. Miao, J. Hu, L. Spinu, D. Ho Kim, and D. Talbayev, Thickness dependent structural, magnetic, and electronic properties of the epitaxial films of transparent conducting oxide $NiCo_2O_4$, J. Appl. Phys. **114**, 103704 (2013).

[27] P. Kang, G. Zhou, H. Ji, Z. Li, Z. Li, and X. Xu, Emergence of room-temperature perpendicular magnetic anisotropy in metallic $NiCo_2O_4$ thin film, J. Magn. Magn. Mater. **553**, 169293 (2022).

[28] P. F. Ndione, Y. Shi, V. Stevanovic, S. Lany, A. Zakutayev, P. A. Parilla, J. D. Perkins, J. J. Berry, D. S. Ginley, and M. F. Toney, Control of the electrical properties in spinel oxides by manipulating the cation disorder, Adv. Funct. Mater. **24**, 610 (2014).

[29] R. Zhang, M. Liu, W. Liu, and H. Wang, Highly conductive n-type $NiCo_2O_{4-\delta}$ epitaxial thin films grown by RF sputtering, Mater. Lett. **199**, 164 (2017).

[30] M. Wang, X. Sui, Y. Wang, Y. H. Juan, Y. Lyu, H. Peng, T. Huang, S. Shen, C. Guo, J. Zhang, Z. Li, H. B. Li, N. Lu, A. T. N'Diaye, E. Arenholz, S. Zhou, Q. He, Y. H. Chu, W. Duan, and P. Yu, Manipulate the electronic and magnetic states in $NiCo_2O_4$ films through electric-field-induced protonation at elevated temperature, Adv. Mater. **31**, 1900458 (2019).

[31] Y. Shen, D. Kan, I. C. Lin, M. W. Chu, I. Suzuki, and Y. Shimakawa, Perpendicular magnetic tunnel junctions based on half-metallic $NiCo_2O_4$, Appl. Phys. Lett. **117**, 042408 (2020).

[32] C. Wu, W. Guo, C. Zhen, H. Wang, G. Li, L. Ma, and D. Hou, Short-range magnetic order and electrical behavior in epitaxial $NiCo_2O_4$ thin films, J. Appl. Phys. **126**, 043901 (2019).

[33] X. Chen, Q. Wu, L. Zhang, Y. Hao, M. G. Han, Y. Zhu, and X. Hong, Anomalous Hall effect and perpendicular magnetic anisotropy in ultrathin ferrimagnetic $NiCo_2O_4$ films, Appl. Phys. Lett. **120**, 242401 (2022).

[34] See Supplemental Material at http://link.aps.org/supplemental/10.1103/PhysRevB.108.094442 for more details. The Supplemental Material includes the results of HAADF-STEM image, XRD patterns, M-H or M-T curves, temperature dependence of the AHE and two-channel AHE model fitting, schematic diagrams, and XPS and XMCD spectra for NCO films.

[35] K. Ueda, M. Mann, P. W. De Brouwer, D. Bono, and G. S. Beach, Temperature dependence of spin-orbit torques across the magnetic compensation point in a ferrimagnetic TbCo alloy film, Phys. Rev. B **96**, 064410. (2017).

[36] L. Caretta, M. Mann, F. Büttner, K. Ueda, B. Pfau, C. M. Günther, P. Hessing, A. Churikova, C. Klose, M. Schneider, D. Engel, C. Marcus, D. Bono, K. Bagschik, S. Eisebitt, and G. S. Beach, Fast current-driven domain walls and small skyrmions in a compensated ferrimagnet, Nat. Nanotechnol. **13**, 1154 (2018).

[37] K. Zhang, C. Zhen, W. Wei, W. Guo, G. Tang, L. Ma, D. Hou, and X. Wu, Insight into metallic behavior in epitaxial half-metallic $NiCo_2O_4$ films, RSC Adv. **7**, 36026 (2017).

[38] C. Zhen, X. Zhang, W. Wei, W. Guo, A. Pant, X. Xu, J. Shen, L. Ma, and D. Hou, Nanostructural origin of semiconductivity

and large magnetoresistance in epitaxial $NiCo_2O_4/Al_2O_3$ thin films, J. Phys. D: Appl. Phys. **51**, 145308 (2018).

[39] A. K. Jaiswal, D. Wang, V. Wollersen, R. Schneider, M. L. Tacon, and D. Fuchs, Direct observation of strong anomalous Hall effect and proximity-induced ferromagnetic state in $SrIrO_3$, Adv. Mater. **34**, 2109163 (2022).

[40] C. F. Windisch Jr, G. J. Exarhos, K. F. Ferris, M. H. Engelhard, and D. C. Stewart, Infrared transparent spinel films with p-type conductivity, Thin Solid Films **398**, 45 (2001).

[41] J. F. Marco, J. R. Gancedo, M. Gracia, J. L. Gautier, E. Ríos, and F. J. Berry, Characterization of the nickel cobaltite, $NiCo_2O_4$, prepared by several methods: An XRD, XANES, EXAFS, and XPS study, J. Solid State Chem. **153**, 74 (2000).

[42] Y. Bitla, Y. Y. Chin, J. C. Lin, C. N. Van, R. Liu, Y. Zhu, H. J. Liu, Q. Zhan, H. J. Lin, C. T. Chen, Y. H. Chu, and Q. He, Origin of metallic behavior in $NiCo_2O_4$ ferrimagnet, Sci. Rep. **5**, 15201 (2015).

[43] M. N. Iliev, P. Silwal, B. Loukya, R. Datta, D. H. Kim, N. D. Todorov, N. Pachauri, and A. Gupta, Raman studies of cation distribution and thermal stability of epitaxial spinel $NiCo_2O_4$ films, J. Appl. Phys. **114**, 033514 (2013).

[44] K. Dileep, B. Loukya, P. Silwal, A. Gupta, and R. Datta, Probing optical band gaps at nanoscale from tetrahedral cation vacancy defects and variation of cation ordering in $NiCo_2O_4$ epitaxial thin films, J. Phys. D: Appl. Phys. **47**, 405001 (2014).

[45] D. Kan, L. Xie, and Y. Shimakawa, Scaling of the anomalous Hall effect in perpendicularly magnetized epitaxial films of the ferrimagnet $NiCo_2O_4$, Phys. Rev. B **104**, 134407 (2021).

[46] A. Gerber, Interpretation of experimental evidence of the topological Hall effect, Phys. Rev. B **98**, 214440 (2018).

[47] D. Kan, T. Moriyama, K. Kobayashi, and Y. Shimakawa, Alternative to the topological interpretation of the transverse resistivity anomalies in $SrRuO_3$, Phys. Rev. B **98**, 180408(R) (2018).

[48] D. Tian, Z. Liu, S. Shen, Z. Li, Y. Zhou, H. Liu, H. Chen, and P. Yu, Manipulating Berry curvature of $SrRuO_3$ thin films via epitaxial strain, Proc. Natl Acad. Sci. USA **118**, e2101946118 (2021).

[49] D. Kan, M. Mizumaki, M. Kitamura, Y. Kotani, Y. Shen, I. Suzuki, K. Horiba, and Y. Shimakawa, Spin and orbital magnetic moments in perpendicularly magnetized $Ni_{1-x}Co_{2+y}O_{4-z}$ epitaxial thin films: Effects of site-dependent cation valence states, Phys. Rev. B **101**, 224434 (2020).

[50] P. Li, C. Xia, J. Li, Z. Zhu, Y. Wen, Q. Zhang, J. Zhang, Y. Peng, H. N. Alshareef, and X. Zhang, Spin filtering in epitaxial spinel films with nanoscale phase separation, ACS Nano **11**, 5011 (2017).

[51] M. Xue, X. Chen, S. Ding, Z. Liang, Y. Peng, X. Li, L. Zha, W. Yang, J. Han, S. Liu, H. Du, C. Wang, and J. Yang, Transport anomaly in perpendicular magnetic anisotropic $NiCo_2O_4$ thin films with column-like phase separation, ACS Appl. Electron. Mater. **2**, 3964 (2020).

[52] Y. Shen, D. Kan, Z. Tan, Y. Wakabayashi, and Y. Shimakawa, Tuning of ferrimagnetism and perpendicular magnetic anisotropy in $NiCo_2O_4$ epitaxial films by the cation distribution, Phys. Rev. B **101**, 094412 (2020).

[53] X. C. Huang, W. W. Li, S. Zhang, F. E. Oropeza, G. Gorni, V. A. de la Peña-O'Shea, T. L. Lee, M. Wu, L. S. Wang, D. C. Qi, L. Qiao, J. Cheng, and K. H. L. Zhang, Ni^{3+}-induced semiconductor-to-metal transition in spinel nickel cobaltite thin films, Phys. Rev. B **104**, 125136 (2021).